Supplementary Information

Dense Packing of Xenon in an Ultra-Microporous Metal-Organic Framework for Benchmark Xenon Capture and Separation

Qiang Liu[1+], Hui-Min Wen[2+], Youjing Gong[1], Jiyan Pei[3], Boyu Liu[1], Shunshun Xiong[1*], Bin Li[3*] and Xiaolin Wang[1*]

[1]Institute of Nuclear Physics and Chemistry, China Academy of Engineering Physics, Mianyang, Sichuan, China.

[2]College of Chemical Engineering, Zhejiang University of Technology, Hangzhou 310014, China.

[3]State Key Laboratory of Silicon Materials, School of Materials Science and Engineering, Zhejiang University, Hangzhou 310027, China.

[+] These authors contributed equally to this work.

*E-mail: ssxiong@caep.cn; bin.li@zju.edu.cn; xlwang@caep.cn

Experimental procedures

Materials

Cupric nitrate trihydrate ($CuNO_3 \cdot 3H_2O$, 98%) and 1,3,5,7-Admantane tetracarboxylic acid (H_4ATC, 99%) were obtained from Sigma-Aldrich, and Sodium hydroxide (NaOH, 90%) was purchased from Sinopharm Chemical Reagent (China). All other chemicals (AR grade) were used as received from commercial suppliers without further purification. Ultrahigh purity grade He (99.999%), CO_2 (99.999%), Xe (99.999%), Kr (99.999%), Ar (99.999%), O_2 (99.999%), N_2 (99.999%), and and a dry gas mixture with Xe (400 ppm) and Kr (40 ppm) balanced with dry air were purchased from WINTEC special gas Co., Ltd. (China) and used for all measurements.

Fitting of single-component adsorption isotherms

The adsorption isotherms for Xe, Kr, N_2, O_2 and Ar in MOF-11 were measured at 273 K, 283 K, 298 K and 308 K. The single-component isotherm data were fitted with the Dual-site Langmuir-Freundlich model:

$$N = N_1^{\max} \times \frac{b_1 p^{1/n1}}{1 + b_1 p^{1/n1}} + N_2^{\max} \times \frac{b_2 p^{1/n2}}{1 + b_2 p^{1/n2}} \quad (1)$$

Where p (unit: kPa) is the pressure of the bulk gas at equilibrium with the adsorbed phase, N (unit: mol/Kg) is the adsorbed amount per mass of adsorbent, $N_1^{\max}$ and $N_2^{\max}$ (unit: mol/Kg) are the saturation capacities of sites 1 and 2, b_1 and b_2 (unit: 1/kPa) are the affinity coefficients of sites 1 and 2, and n_1 and n_2 represent the deviations from an ideal homogeneous surface. Here, the single-component Xe, Kr, O_2, N_2 and Ar adsorption isotherms have been fit to enable the application of IAST in simulating the performance of porous materials, under a mixed component gas. The fitting parameters of DSLF equation are listed in Table S1.

IAST calculations

The adsorption selectivity was established by the Ideal Adsorbed Solution Theory (IAST) for Xe/Kr (20/80, v/v), Xe/Ar (1/99, v/v), Xe/N_2 (1/99, v/v), Xe/O_2 (1/99, v/v) binary gas

mixtures in MOF-11. The adsorption selectivity is defined by the following equation:

$$S_{A/B} = \frac{X_A/X_B}{Y_A/Y_B} \qquad (2)$$

Where X_A and X_B are the mole fractions of the gases A and B in the adsorbed phase and Y_A and Y_B are the mole fractions of the gases A and B in the bulk phase.

Calculation of Isosteric heat of adsorption and Henry's constant

Determination of the heat of adsorption at zero surface coverage, which is a fundamental measure of the adsorbate–adsorbent interaction, can be calculated by analysis of the isotherms using the virial equation, which has the form

$$\ln\left(\frac{n}{p}\right) = A_0 + A_1 n + A_2 n^2 + \cdots \qquad (3)$$

where p is pressure, n is the amount adsorbed and A_0, A_1, A_2, etc., are virial coefficients. At low surface coverage, A_2 and A_3 can be neglected. Plotting ln(n/p) gives a straight line graph with the gradient A_1 describing adsorbate–adsorbate interactions and the intercept A_0 describing adsorbate–adsorbent interactions. At low surface coverage, the virial equation reduces to Henry's Law. However, the A_1 parameter for isotherms in the range 273 K–308 K was very small at low surface and the isotherms were linear following Henry's Law:

$$n = K_H P \qquad (4)$$

Where n is amount adsorbed, K_H is the Henry's law constant and P is the pressure. Adherence to Henry's Law is indicative of weak interactions between adsorbate molecules at low surface coverage. The low range of the adsorption isotherm is nearly linear which corresponds to Henry's law behavior. The Henry's constant for reported materials in this work were obtained from a linear fit to the in low pressure part of the isotherms.

Thus the isosteric heat at zero surface coverage of Xe and Kr for MOF-11 was calculated using the following equation:

$$Q_{st,n=0} = RT^2\left(\frac{\partial \ln K_H}{\partial T}\right)_n \qquad (5)$$

Where $Q_{st,n=0}$ is the isosteric enthalpy of adsorption at zero surface coverage, T is the temperature, R is the universal gas constant and K_H is the Henry constant. Therefore, the

gradient of ln(K_H) vs. 1/T, at constant amount adsorbed, is equal to Q_{st}/R.

The adherence of the xenon isotherms to the Henry's Law region in the temperature range 268–298 K is shown in Fig. S9 and Fig S13. The isotherms at 273 K, 283 K, 298 K and 308 K are linear over the range 0–25.0 mbar (0–1000 Pa). The K_H constants are tabulated in Table S2 and Table S3.

The isosteric heat of adsoprtion values (Q_{st}) for different gases in this work were calculated by the Clausius-Clapeyron equation. The heat enthalpy of Xe and Kr are determined by the adsorption isotherms of Kr and Xe at 273 K, 283 K, 298 K and 308 K. The heat enthalpy of N_2, O_2 and Ar sorption for MOF-11 in this manuscript are determined by using the sorption data measured at 298 K and 273 K in the pressure range from 0-100 kPa.

$$\frac{Q_{st}}{R} = \frac{d(\ln P)}{d(1/T)} \qquad (6)$$

Where X_A and X_B are the mole fractions of the gases A and B in the adsorbed phase and Y_A and Y_B are the mole fractions of the gases A and B in the bulk phase.

Tables

Supplementary Table 1. Dual-Langmuir-Freundlich fitting parameters for adsorption isotherms of Xe, Kr, N_2, O_2 and Ar in MOF-11.

Adsorbates	Temperature	N_1^{max}	b_1	n_1	N_2^{max}	b_2	n_2	R^2
Xe	308 K	1.548	0.0501	1.960	4.462	0.101	0.887	0.999
	298 K	1.662	0.0568	1.908	4.458	0.158	0.862	0.999
	283 K	1.973	0.177	1.575	3.735	0.306	0.789	0.999
	273 K	3.643	0.552	0.763	2.035	0.273	1.585	0.999
Kr	308 K	4.982	0.00786	1.041	0.1503	0.00101	0.502	0.999
	298 K	4.417	0.00889	1.072	1.116	0.00828	0.869	0.999
	283 K	5.167	0.145	0.981	0.3799	0.3799	0.334	0.999
	273 K	5.334	0.0213	1.004	0.0446	0.00151	0.499	0.999
Ar	298 K	3.728	0.00101	0.999	2.631	0.00151	1.093	0.999
	273 K	1.704	0.00563	1.070	3.681	0.00102	0.921	0.999
N_2	298 K	6.308	0.00216	1.107	0.0778	0.00164	0.532	0.999
	273 K	20.72	3.91E-4	1.122	1.650	0.0139	0.980	0.999
O_2	298 K	13.32	4.42E-5	0.743	0.527	0.0125	1.061	0.999
	273 K	3.719	0.00323	1.018	0.4495	1.002E-5	0.521	0.999

Supplementary Table 2. Henry's Law constants for Xe adsorption on MOF-11 at 273, 283, 298 and 308 K.

Temperature (K)	K_H (mmol g^{-1} kPa^{-1})	Ln(K_H) (ln(mmol g^{-1} k Pa^{-1}))
273	2.12	0.7514
283	1.33	0.2852
298	0.695	-0.3638
308	0.492	-0.7093

Supplementary Table 3. Henry's Law constants for Kr adsorption on MOF-11 at 273, 283, 298 and 308 K.

Temperature (K)	K_H (mmol g^{-1} kPa^{-1})	Ln(K_H) (ln(mmol g^{-1} k Pa^{-1}))
273	0.108	-2.226
283	0.0766	-2.569
298	0.0438	-3.128
308	0.0341	-3.378

Supplementary Table 4. Crystal data and structure refinement for Xe loaded MOF-11.

CCDC Number	2130314	
Chemical formula	$C_{14}H_{12}Cu_2O_8Xe_3$	
Formula weight	829.22	
Radiation	Mo K_α	
Wavelength (Å)	0.71073	
Crystal system, space group	tetragonal, $P_{42/mcc}$	
Unit cell parameter	a = 8.4421(7) Å	α = 90°
	b = 8.4421(7) Å	β = 90°
	c = 14.4874(19) Å	γ = 90°
Volume (Å^3)	1032.5(2)	
Z, Calculated density (g/cm^3)	2, 2.667	
F(000)	760	
Crystal size (mm)	0.24×0.2×0.18	
Completeness (to theta)	0.969	
Refinement method	SHELXL-2018	
Goodness-of-fit on F^2	1.193	
Final R indices (I>2sigma(I))	R_1 = 0.1144, wR_2 = 0.2800	

Supplementary Table 5. Comparison of Xe capture (298 K) and separation properties in this work with reported porous materials.

Materials	Xe uptake (mmol/g)		Xe/Kr	Pore	Xe Q_{st}	Density	ref
	0.2bar	1bar	Selectivity	Size (Å)	(kJ/mol)	(g/cm^3)	
MOF-11	4.0	4.96	19.1[b]	~4.3	29.4	1.41	This work
ZU-62	0.19	3.77	N.A.	5.0	N.A.	1.62	1
PAF-67	1.115	2.8	6.6[c]	~5.0	28.6	N.A.	2
PAF-45	1.08	2.21	8.1[c]	~5.0	27.6	N.A.	2
CTF-0	0.355	1.125	5.2[c]	~5.0	25.7	N.A.	3
NU-403	0.50	1.7	2.84[b]	9.5	22.0	1.42	3
UiO-66	0.71	1.98	5.9[b]	9.3, 12.1	24.6	1.26	3
$(Sr_4(TCPE)_2)$	0.37	0.85	7[b]	5.2	19.4	1.32	4
IISERP-MOF2	2.84	3.2	6.5[b]	4.7	32	1.25	5
ECUT-60	2.30	4.3	11.36[b]	3.8×5.2	30	N.A.	6
$Zn(ox)_{0.5}(trz)$	2.06	2.72	10.2[b]/12.5[c]	4.02	29	1.59	7
Co-squarate	≈1.18	1.35	69.7[b]	4.1×4.3	43.6	2.19	8
MOF-Cu-H	2.66	3.2	16.7[b]	4.4	33.4	1.27	9
MOF-74-Co	2.59	6.0	11.8[b]	11	28.3	1.17	10
MOF-74-Ni	2.59	5.6	10.1[b]	11	27.3	1.17	10
Ag-MOF-303	1.83	3.5	10.4[b]	5.2	28.2	1.44	11
SIFSIX-3-Zn	1.85	3.09	9.2[b]	3.8	30.0	1.59	12
$Co_3(HCOO)_6$	1.35	2	12[b]	4.2	28	1.82	13
NKMOF-1-Ni	1.35	2.17	5.2[b]	5.4	34.2	1.75	14
SBMOF-1	1.27	1.47	16[b]	5.0	37	1.55	15
SBMOF-2	1.46	2.85	10[b]	6.5	26.4	1.19	16
Zr-Fum-Me	1.03	1.91	11.7[b]	5.2, 5.5	30.9	1.73	17
MIL-120	1.42	1.99	9.6[b]	5.4×4.7	31.5	1.57	18
SIFSIX-3-Fe	1.38	2.44	N.A.	3.7	27.4	1.52	19
Zr-Fum (MOF-801)	0.88	1.89	8.3[b]	6.6, 6.9	25.3	1.63	17
CROFOUR-1-Ni	1.11	1.79	22[b]	N.A.	37.4	1.17	20
MOF-303	1.26	4.15	6.6[b]	8.7	23.7	0.99	11
Ca-SINAP-1	1.646[a]	2.87[a]	10.32[c]	~4.8 × 13.6	29.2	1.173	21
ECUT-50	0.94	2.26	8[b]	8.0 ×3.5 7.2 × 3.9	32	1.139	22
ZIF-69	0.9	2.46	8.35[c]	7.2	24.93	N.A.	23
Co^{2+}-CPM-6	1.06	3.0	9.3[b]	6.0, 7.5	25.9	1.18	24
UTSA-74	0.93	2.70	8.4[b]	10.0	24.4	1.34	25
CC3	1.66	2.44	20.4[d]	4.4	31.3	0.97	26

Al-Fum	1.52	3.47	8.1[b]	5.6	22.4	0.99	27
Al-Fum-Me	1.75	3.01	10.0[b]	5.3	32.4	1.08	27

[a] Xe uptake at 293 K

[b] IAST selectivity of 20/80 Xe/Kr binary gas mixture at 298 K and 1 bar

[c] Xe/Kr selectivity calculated by Henry constants

[d] From breakthrough experiment (400 ppm Xe and 40 ppm Kr in air)

Figures

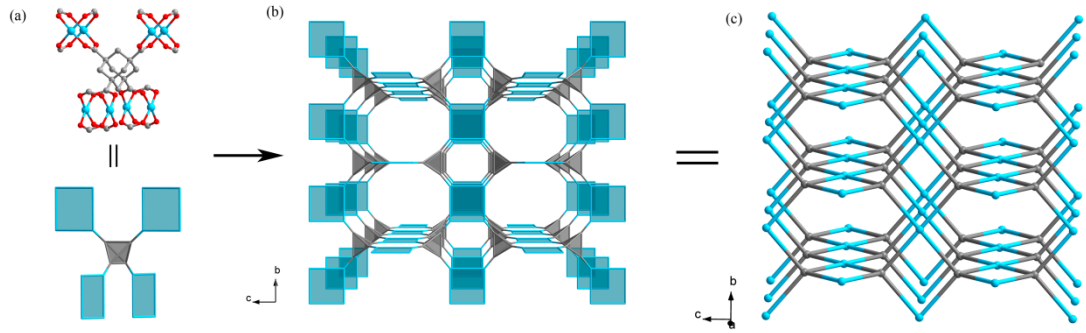

Supplementary Figure 1. The ATC^{4-} linker and $Cu_2(COO)_4$ paddle-wheel building unit can be represented as four connect-nodes (a). The crystal structure of MOF-11 can be simplified as a (4,4)-connected PtS topology network (b) and (c).

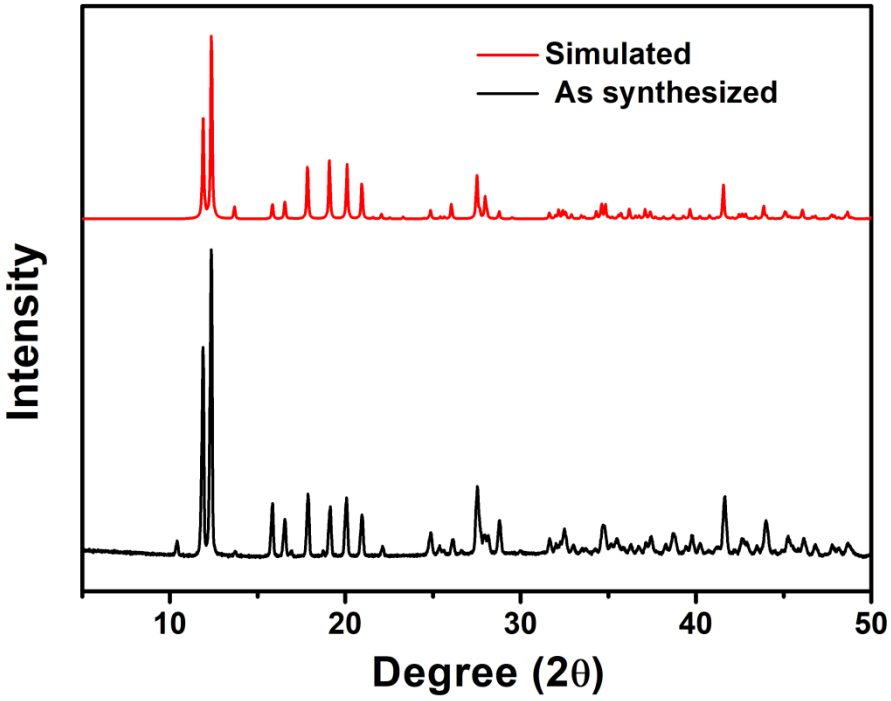

Supplementary Figure 2. The calculated and synthesized PXRD patterns of MOF-11.

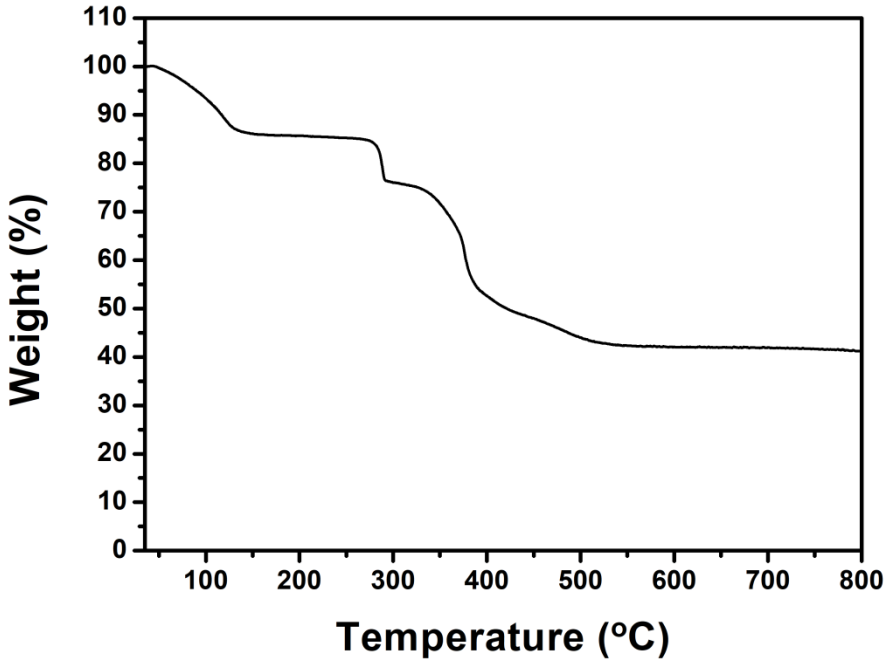

Supplementary Figure 3. The TGA curve of as-synthesized MOF-11 samples from room temperature to 800 °C.

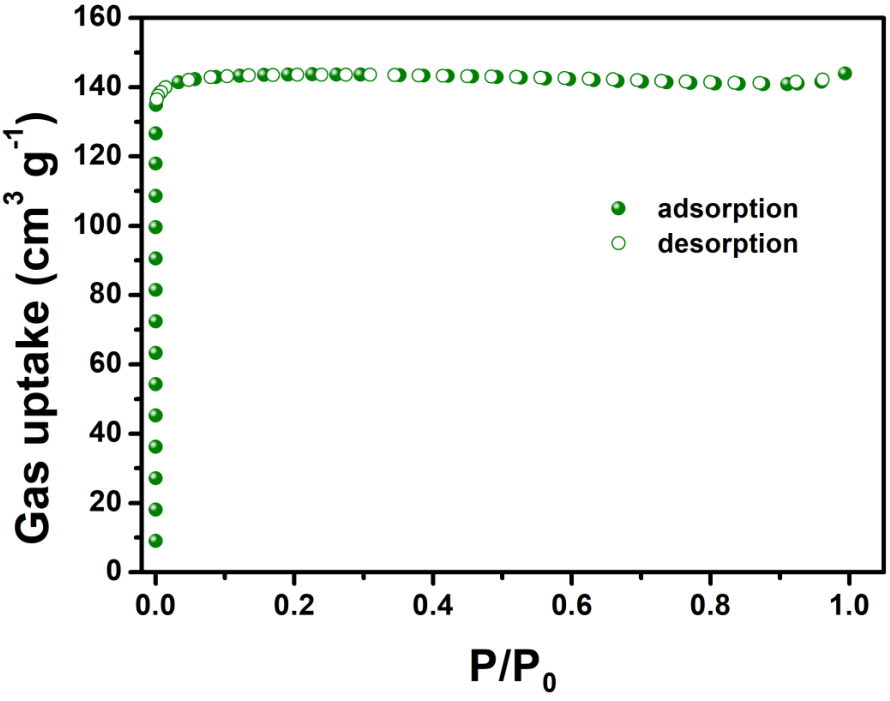

Supplementary Figure 4. N_2 sorption isotherms of MOF-11 at 77K.

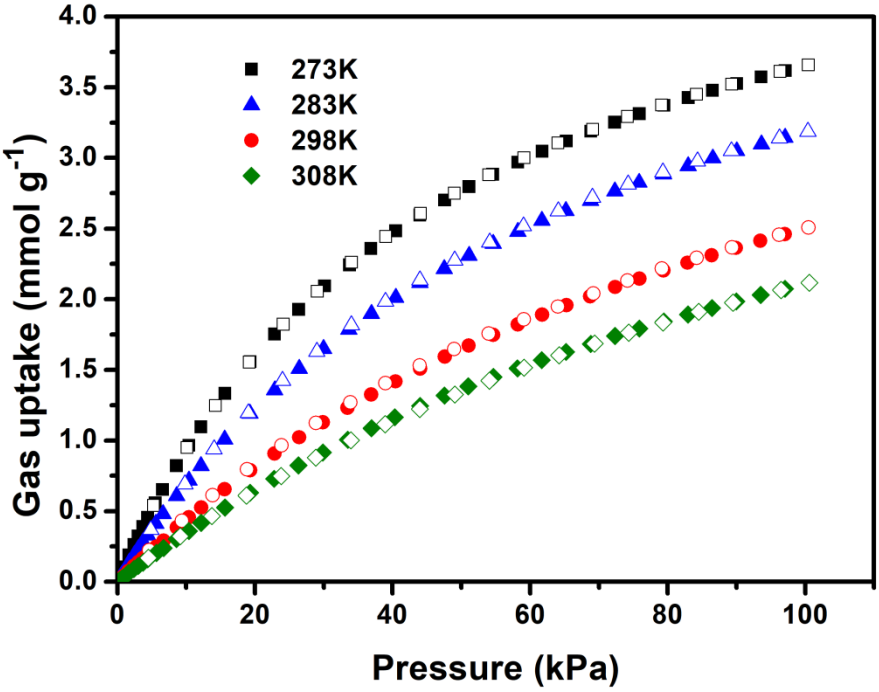

Supplementary Figure 5. Kr sorption isotherms of MOF-11 at 273 K, 283 K, 298 K and 308 K.

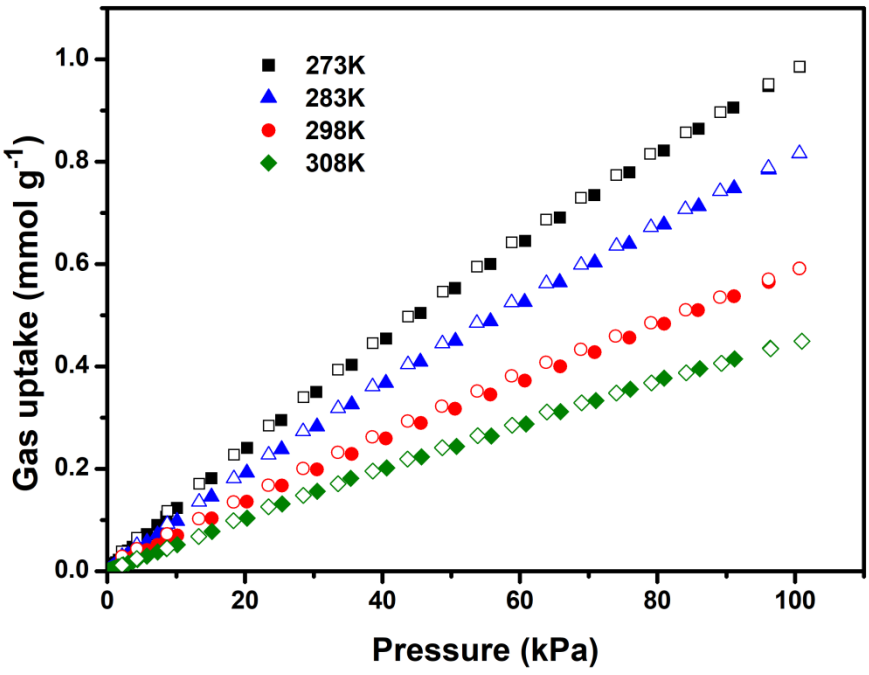

Supplementary Figure 6. Ar sorption isotherms of MOF-11 at 273 K, 283 K, 298 K and 308 K.

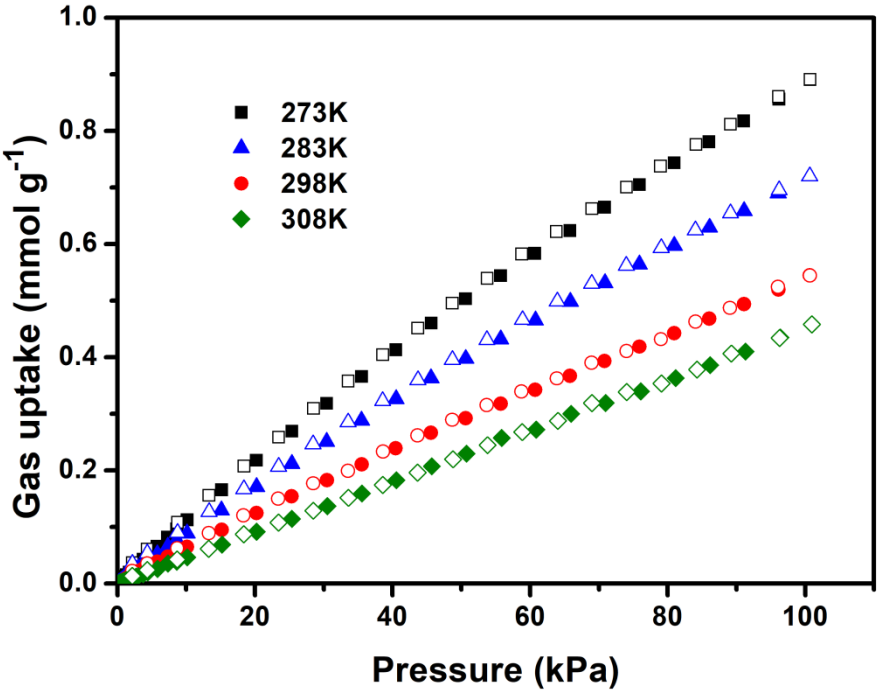

Supplementary Figure 7. O_2 sorption isotherms of MOF-11 at 273 K, 283 K, 298 K and 308 K.

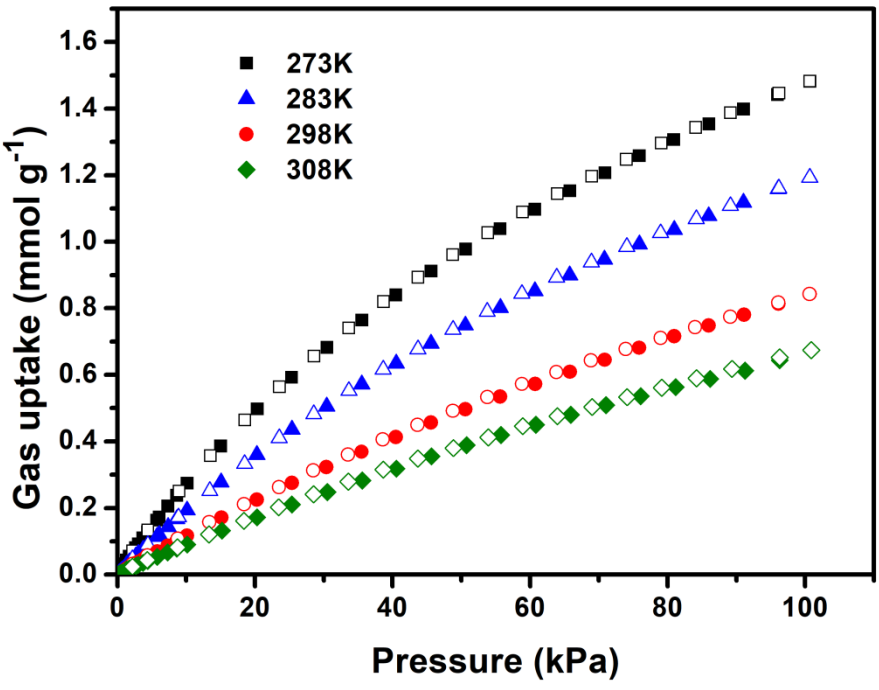

Supplementary Figure 8. N_2 sorption isotherms of MOF-11 at 273 K, 283 K, 298 K and 308 K.

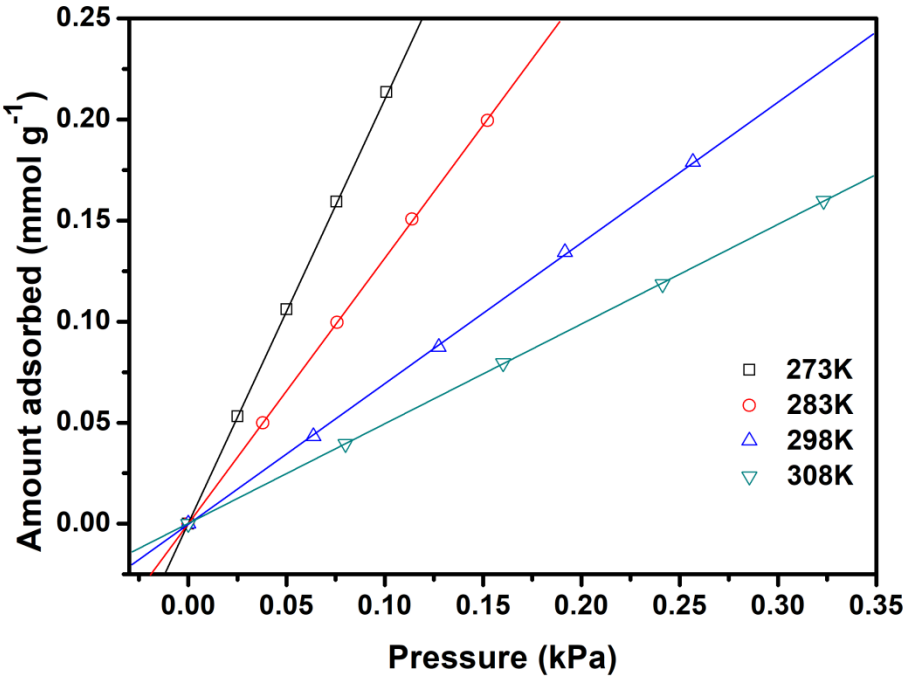

Supplementary Figure 9. Henry's Law region, covering the pressure range 0–350 Pa, for the Xe isotherms at 273 K, 283 K, 298 K and 308 K.

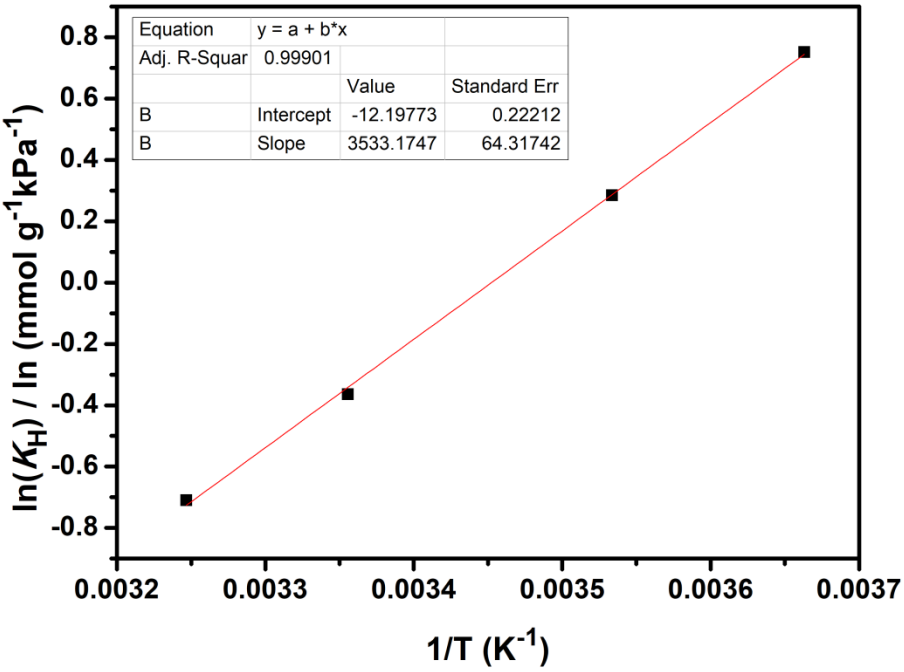

Supplementary Figure 10. Graph of ln(K_H) vs. 1/T for Xe adsorption on MOF-11 for 273 K, 283 K, 298 K and 308 K for calculation of Q_{st} at zero surface coverage (Q_{st} = 29.37 ± 0.53 kJ mol^{-1}).

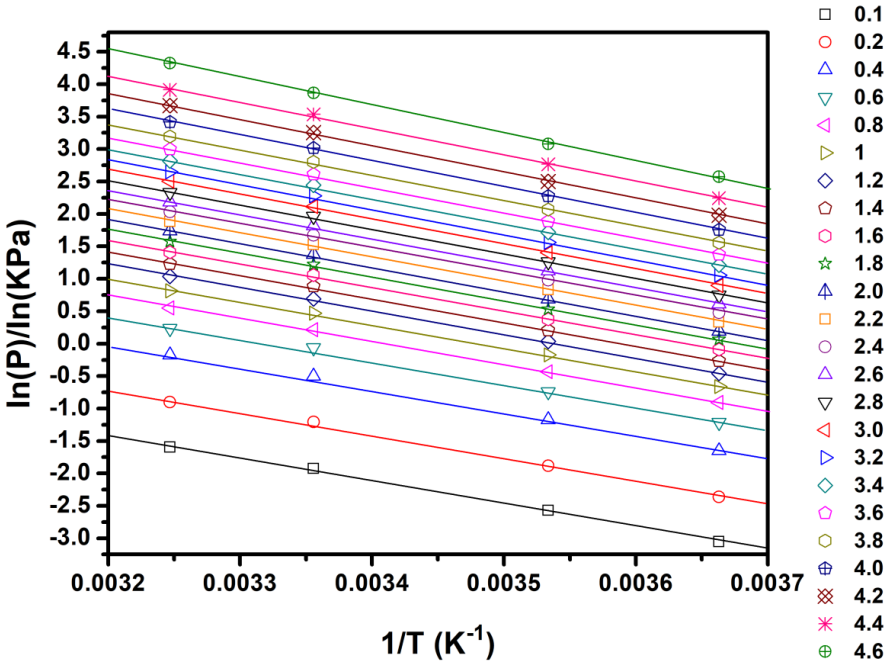

Supplementary Figure 11. Van't Hoff isochore graphs for Xe adsorption on MOF-11 for temperatures 273 K, 283 K, 298 K and 308 K, as a function of the amount adsorbed (n) ranging from 0.1–4.6 mmol g^{-1}.

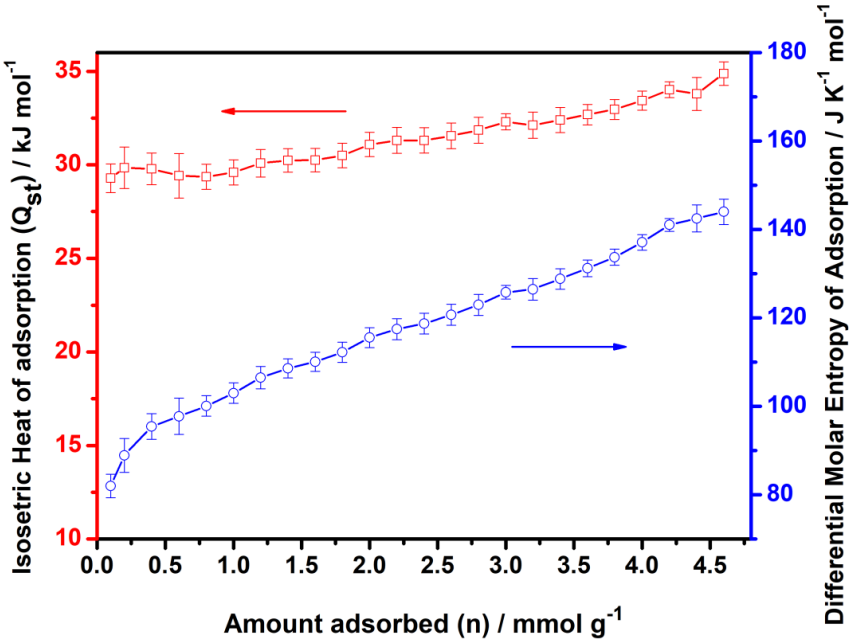

Supplementary Figure 12. Isosteric heat (Q_{st}/kJ mol^{-1}) and differential molar heat (ΔS/J K^{-1} mol^{-1}) of adsorption for Xe as a function of the amount adsorbed (mmol g^{-1}) for the temperature range 273–308 K.

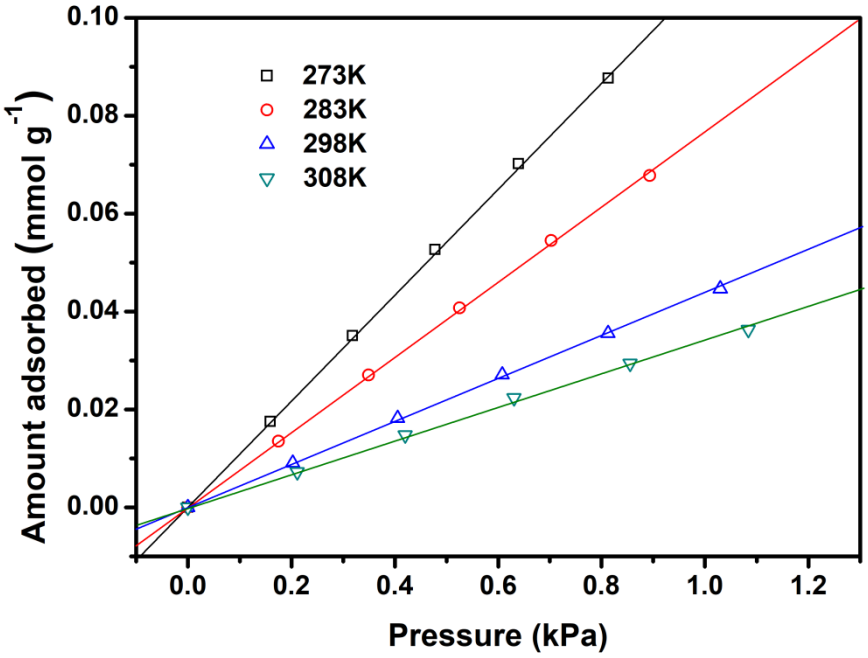

Supplementary Figure 13. Henry's Law region, covering the pressure range 0–1000 Pa, for the Kr isotherms at 273 K, 283 K, 298 K and 308 K.

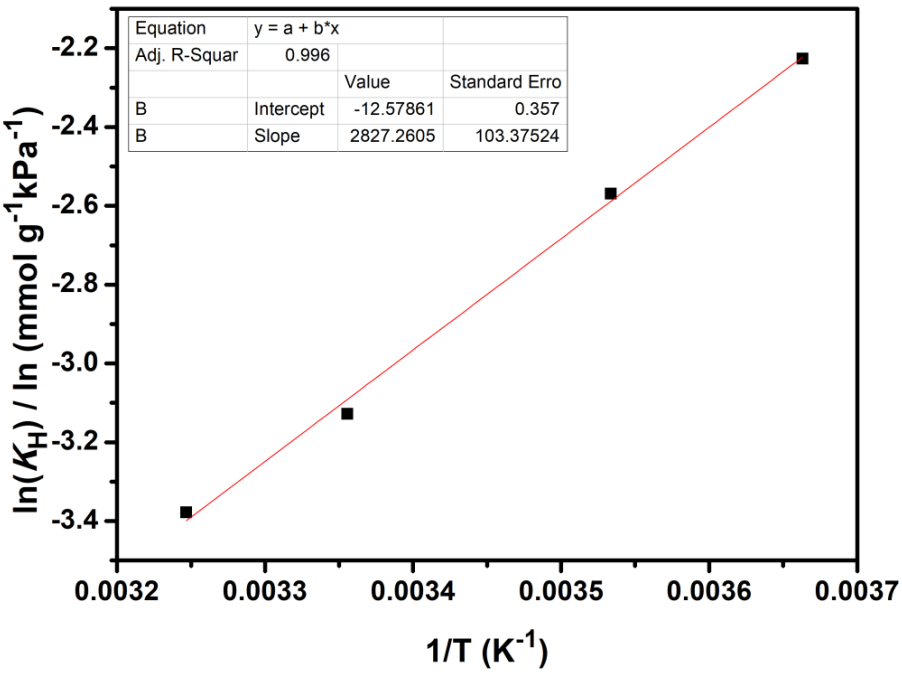

Supplementary Figure 14. Graph of ln(K_H) vs. 1/T for for krypton adsorption on MOF-11 for 273 K, 283 K, 298 K and 308 K for calculation of Q_{st} at zero surface coverage (Q_{st} = 23.51 ± 0.86 kJ mol^{-1}).

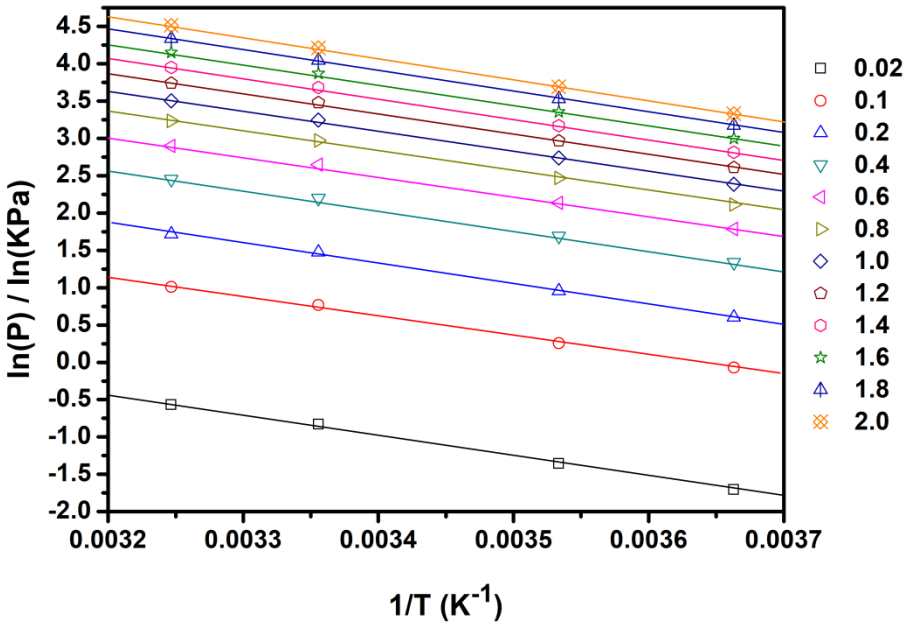

Supplementary Figure 15. Van't Hoff isochore graphs for Kr adsorption on MOF-11 for temperatures 273 K, 283 K, 298 K and 308 K, as a function of the amount adsorbed (n) ranging from 0.02–2.0 mmol g^{-1}.

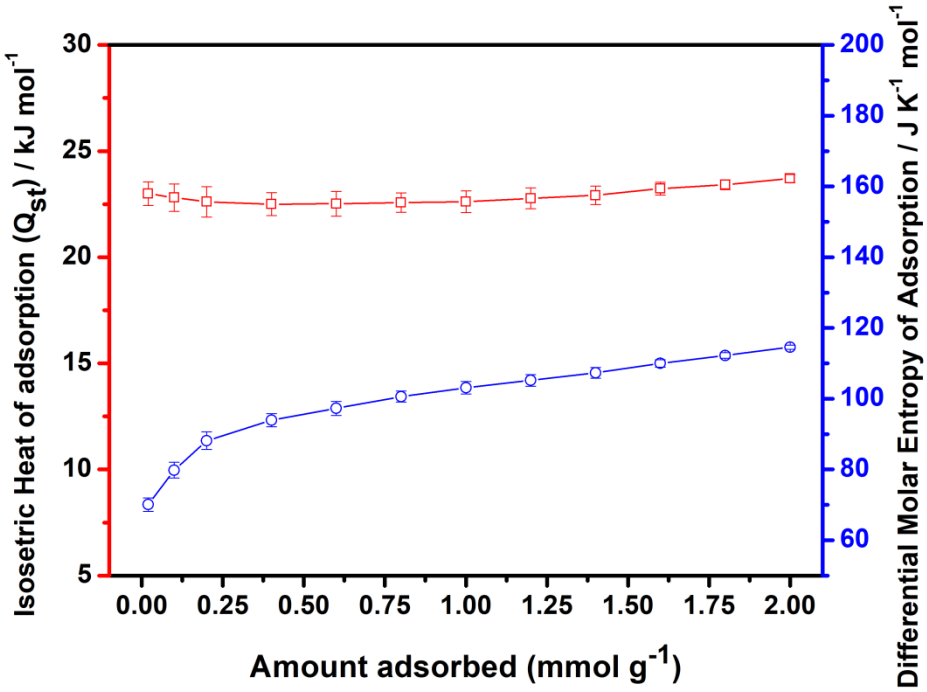

Supplementary Figure 16. Isosteric heat (Q_{st}/kJ mol^{-1}) and differential molar heat (ΔS/J K^{-1} mol^{-1}) of adsorption for Kr as a function of the amount adsorbed (mmol g^{-1}) for the temperature range 273–308 K.

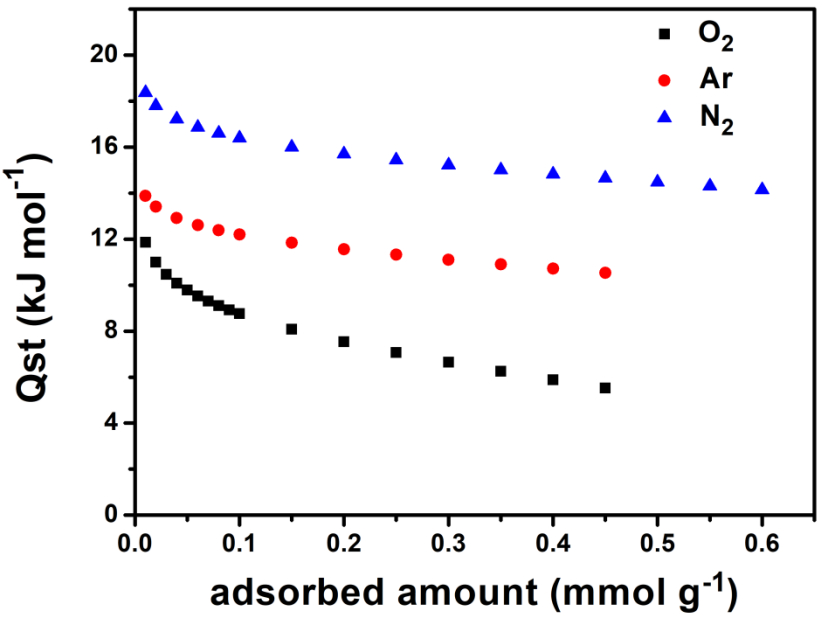

Supplementary Figure 17. Isosteric heat (Q_{st}/kJ mol^{-1}) of adsorption for N_2, O_2 and Ar as a function of the amount adsorbed (mmol g^{-1}).

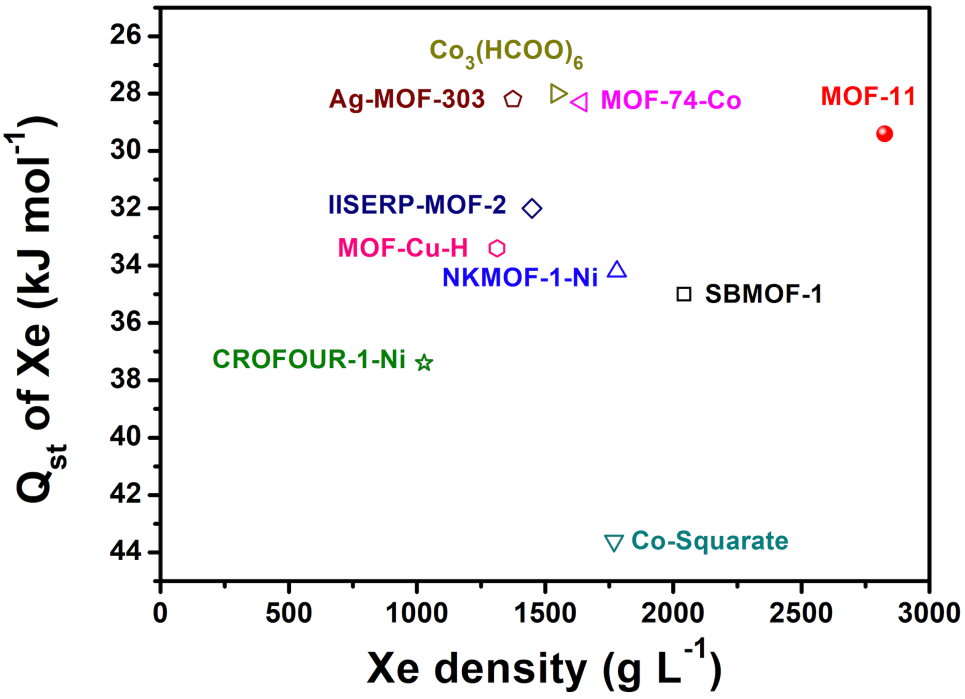

Supplementary Figure 18. Comparison of Xe density at 1 bar and room temperature and Q_{st} of Xe for MOF-11 and other Xe/Kr separation MOFs.

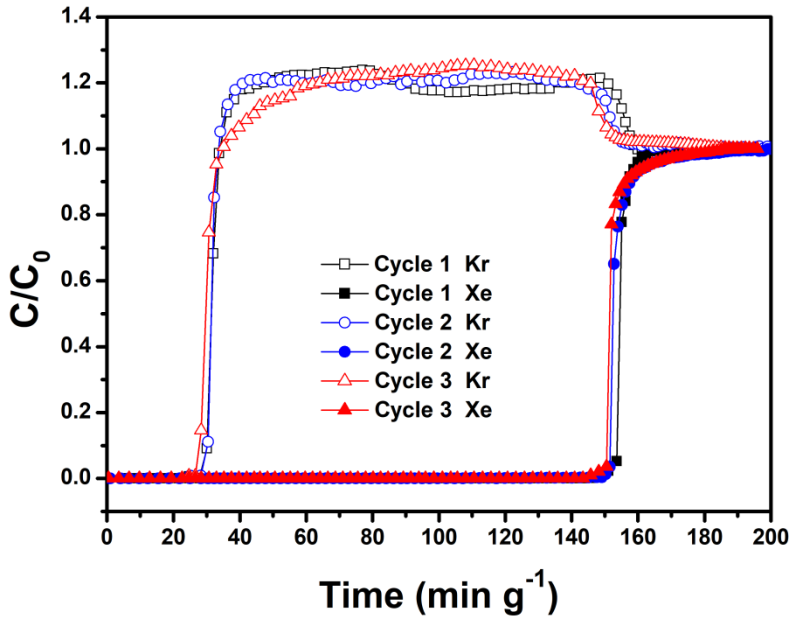

Supplementary Figure 19. Experimental column breakthrough curves for a cycling test of 20/80 Xe/Kr mixture with a total flow of 2.5 mL min^{-1} in an absorber bed packed with MOF-11 at 298 K and 1 bar.

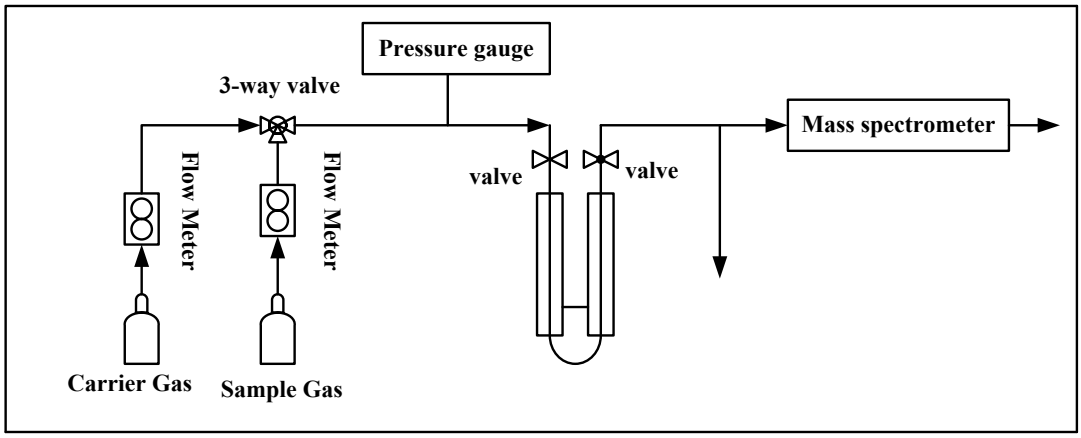

Supplementary Figure 20. Representation of the dynamic breakthrough experiment.

Supplementary References:

1. Wang, Q. *et al*. Separation of Xe from Kr with Record Selectivity and Productivity in Anion-Pillared Ultramicroporous Materials by Inverse Size-Sieving. *Angew*. *Chem*. *Int*. *Ed*. **132**, 3451–3456 (2020).
2. Li, H. *et al.* Ultramicroporous organic materials for selective separation of xenon from krypton. *Micropor Mesopor Mat*. **305**, 110390–110395 (**2020)**.
3. Idrees, K. B. *et al.* Tailoring Pore Aperture and Structural Defects in Zirconium-Based Metal–Organic Frameworks for Krypton/Xenon Separation. *Chem Mater.* **32**, 3776–3782 (2020),.
4. Xiong, J. *et al.* Creating uniform pores for xenon/ krypton and acetylene/ethylene separation on a strontium-based metal-organic framework. *J. Solid. State. Chem.* **288**, 121337 (2020)**.**
5. Chakraborty, D. *et al.* An Ultra-Microporous Metal–Organic Framework with Exceptional Xe Capacity. *Chem. Eur. J.* **26**, 12544–12548 (2020).
6. Zhang, H. *et al.* Robust metal–organic framework with multiple traps for trace Xe/Kr separation. *Science Bulletin* **66**, 1073-1079 (2021**)**.
7. Yu, L. *et al.* Tuning the Channel Size and Structure Flexibility of Metal-Organic Frameworks for the Selective Adsorption of Noble Gases. *Inorg. Chem.* 58, 15025–15028 (2019).
8. Li, L. *et al.* A Robust Squarate-Based Metal–Organic Framework Demonstrates Record-High Affinity and Selectivity for Xenon over Krypton. *J. Am. Chem. Soc.* 141, 9358–9364 (2019)..
9. Xiong, S. *et al.* A microporous metal–organic framework with commensurate adsorption and highly selective separation of xenon. *J. Mater. Chem. A* **6**, 4752–4758 (2018).
10. Kapelewski, M. T. *et al*. Separation of Xenon and Krypton in the Metal–Organic Frameworks M_2(m-dobdc) (M = Co, Ni). *Isr. J. Chem.* **58**, 1138–1143 (2018).
11. Wang, H. *et al.* Docking of CuI and AgI in Metal–Organic Frameworks for Adsorption and Separation of Xenon. *Angew. Chem. Int. Ed.* **60**, 3417–342 (2021).
12. Liu, Y., *et al.* Noble gas separation by a MOF with one-dimensional channels. *BMC Chem. Eng.* **1**, 3 (2019).
13. Wang, H. *et al.* The first example of commensurate adsorption of atomic gas in a MOF and effective separation of xenon from other noble gases. *Chem. Sci.* **5**, 620–624 (2014).
14. Wang, T. *et al.* Robust Bimetallic Ultramicroporous Metal–Organic Framework for Separation and Purification of Noble Gases. *Inorg. Chem.* **59**, 4868–4873 (2020**)**.
15. Banerjee, D. *et al.* Metal-organic framework with optimally selective xenon adsorption and separation. *Nat. Commun.* **7**, 11831–11837 (2016).
16. Chen, X. *et al.* Direct observation of Xe and Kr adsorption in a Xe-selective microporous metal-organic framework. *J. Am. Chem. Soc.* **137**, 7007–7010 (2015).
17. Yan, Z. *et al.* Methyl functionalized Zr-Fum MOF with enhanced Xenon adsorption and separation. *Sep. Purif. Techol.* **239**, 116514 (2020).
18. Zhang, P. *et al.* Robust Ultramicroporous Metal–Organic Framework with Rich Hydroxyl-Decorated Channel Walls for Highly Selective Noble Gas Separation. *Chem. Eng.*

Dat. **65**, 4018–4023 (**2020)**.
19. Elsaidi, S. K. *et al*. Effect of ring rotation upon gas adsorption in SIFSIX-3-M (M = Fe, Ni) pillared square grid networks. *Chem. Sci.* **8**, 2373–2380 (2017).
20. Mohamed, M. H. *et al.* Hybrid ultra-microporous materials for selective xenon adsorption and separation, *Angew. Chem. Int. Ed.* **55**, 8285–8289 (2016).
21. Wu, X.-L. *et al.* Enhanced Adsorption and Separation of Xenon over Krypton via an Unsaturated Calcium Center in a Metal-Organic Framework. *Inorg Chem*. **60**, 1506-1512 (2021).
22. Wang, L. *et al.* A Robust Calcium–Organic Framework for Effective Separation of Xenon and Krypton. *Cryst. Growth Des*. **21**, 954-959 (2021).
23. Luo, S. et al. Uptake and separation of Xe and Kr by a zeolitic imidazolate framework with a desirable pore window. *J. Radioanal. Nucl. Chem.* **324**, 1275–1281 (2020).
24. Liu, B. *et al.* Enhanced xenon adsorption and separation with an anionic indium–organic framework by ion exchange with Co^{2+}. *RSC Adv*. **7**, 55012–55019 (2017).
25. Tao, Y. *et al.* Boosting Selective Adsorption of Xe over Kr by Double-Accessible Open-Metal Site in Metal–Organic Framework: Experimental and Theoretical Research. *Inorg. Chem.* **59**, 11793–11800 (2020).
26. Chen, L. *et al.* Separation of rare gases and chiral molecules by selective binding in porous organic cages. *Nat. Mater.* **13**, 954–960 (2014).
27. Yan, Z. *et al.* Pore Size Reduction by Methyl Function in Aluminum-Based Metal–Organic Frameworks for Xenon/Krypton Separation. *Cryst. Growth Des.* **20**, 8039–8046 (2020).